1 **Supporting Information for**

2 **Generation, Control, and Application of Stable Bubble in Hypersonic Acoustic**

3 **System**

4 **Xiaotian Shen[a], Xianwu Ke[a], Tiechuan Li[a], Chongling Sun[a], and Xuexin Duan[a,*]**

5 *[a] State Key Laboratory of Precision Measuring Technology and Instruments, School of Precision*

6 *Instrument and Opto-electronics Engineering, Tianjin University, Tianjin 300072, China.*

7 * Corresponding author. E-mail: xduan@tju.edu.cn

8 1 Structure of bulk acoustic device and system setup

9   The schematic of structure of bulk acoustic wave device was shown in Figure S1. The system

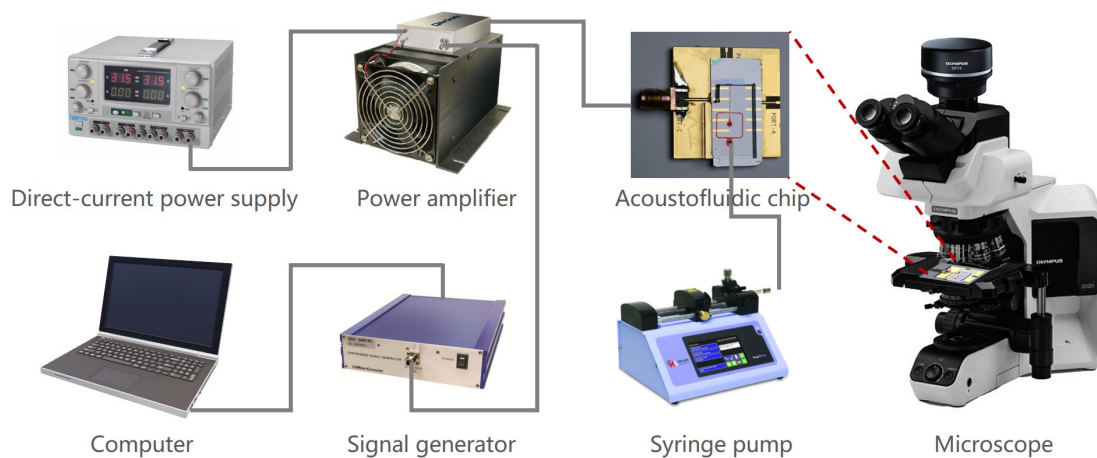10 setup was shown in Figure S2.

11
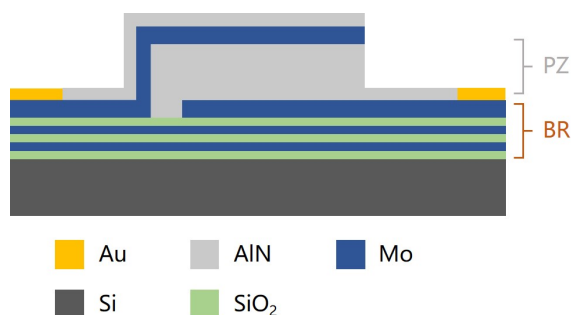
12

13 Figure S1. The schematic of the BAW device structure. BR represents the Bragg reflector structure. PZ represents
14 the piezoelectric structure.

15

16
17 Figure S2. Setup of the hypersonic acoustic system.
18

2 Roughening treatment of the surface of BAW device

The device was protected by depositing a thin film of aluminum nitride (AlN) as passivation (PS) layer with the thickness of 200 nm. The PS layer was etched by positive photoresist for 10, 20, 30 and 120 s respectively. The roughness of the device surface was measured by AFM. The RMS roughness increased with the increase of etching time. When the etching time was greater than 30 s, the RMS roughness tended to level off (Figure S3). However, the peak-to-valley roughness Rt was about 320 nm at the etching time of 30 s, which was larger than the thickness of PS layer. That meant there was a great risk that the top electrode would be exposed to air, resulting in the oxidation and invalidation. Thus, 20 seconds was a proper etching time to treat the device and maintain the effectiveness of device.
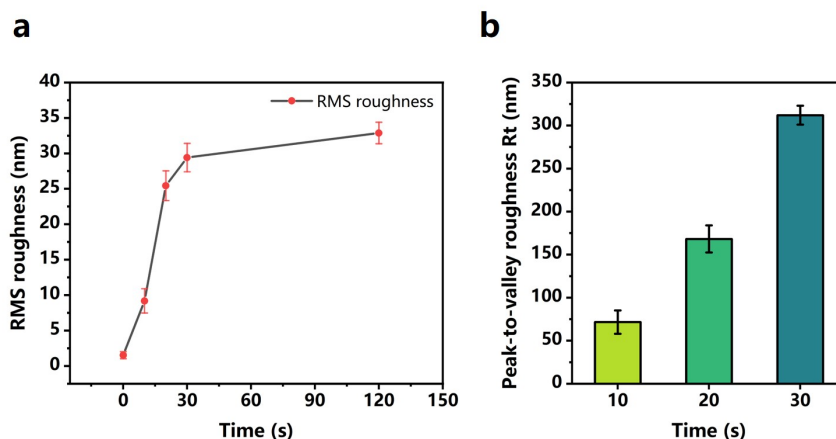
Figure S3 Roughness characterization of the device surface with AFM. (a) The RMS roughness versus different etching times. (b) The peak-to-valley roughness versus different etching times.

3 Acoustothermal effect of hypersonic acoustic system

The acoustothermal effect of gigahertz bulk acoustic waves (GHz BAWs) in the oil phase is non-negligible, especially when high power is applied. To characterize the temperature distribution of GHz BAWs in oil, pyrromethene 597 was employed as a temperature-sensitive indicator. The pyrromethene 597 was dissolved in the mineral oil with 1.5 wt. % Span 80 at the concentration of 0.129 mg mL^{-1}. The device covered with the microfluidic chip was placed on a hot plate. The device temperature was

40 measured by the thermocouple. The mineral oil seeded with temperature-sensitive fluorescence dye

41 was pumped into the microchannel. The fluorescence intensity of oil phase at different temperatures

42 was recorded by the microscopy (Figure S4a). The inner circular region of the pentagon device was

43 chosen as region of interest (ROI) to extract the fluorescence intensity. The calculation curve of

44 intensity versus temperature was obtained in Figure S4b, which could be used to characterize the

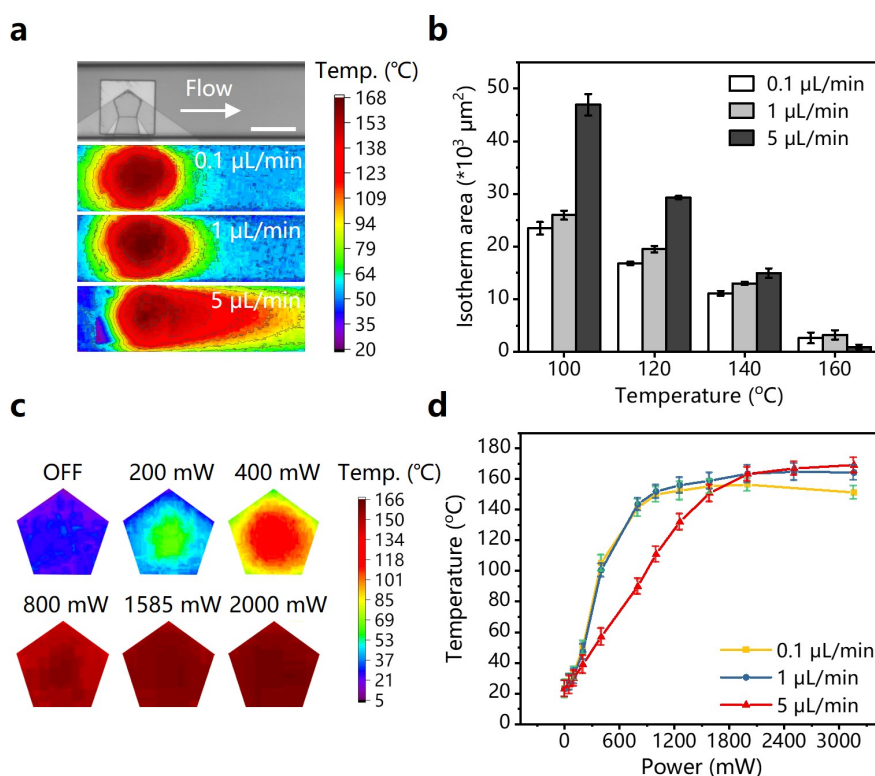45 acoustothermal effect of GHz BAWs in oil.

46
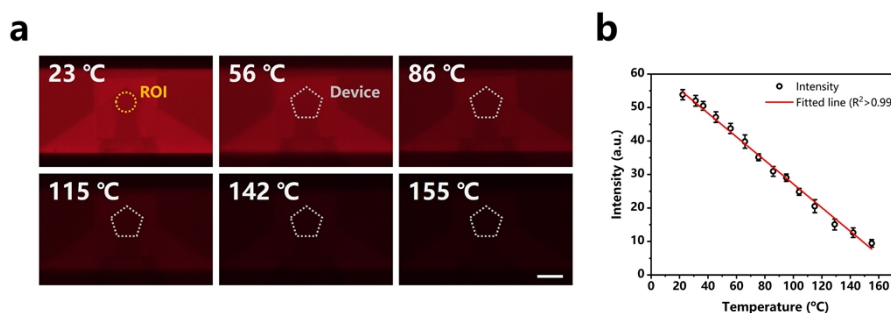
47

48 Figure S4 Characterization of the relation between the fluorescence intensity and temperature. (a) The fluorescent

49 images at different temperatures. (b) The calibration curve between the temperature and intensity. The scale bar is 50

50 μm.

51

52   The dynamic changes and temperature distribution in the oil phase were tested experimentally at

53 different applied powers and flow rates to further examine the acoustothermal effect induced by GHz

54 BAWs. The real-time changes in oil temperature were determined by analysis of the fluorescence

55 intensity with reference to the calibration curve. First, the impact of the flow rate of the oil phase on

56 the temperature distribution was investigated. The temperature distribution at an applied power of 2000

57 mW at the flow rates of 0.1, 1, and 5 μL min^{-1}, respectively, in the microchannel were measured. As

58 the flow rate increased, the temperature distribution shifted downstream and expanded (Figure S5a).

59 A fast-flowing oil phase enhanced heat diffusion in the microchannel. Next, the areas of different

60 isotherms were calculated to determine the expansion of the temperature distribution at high flow rates

61 (Figure S6). The areas of the isotherms at 100 °C, 120 °C, and 140 °C at a flow rate of 5 μL min^{-1} were

62 larger than those of the isotherms at lower flow rates. In addition, the area of the isotherm at 160 °C at

63 a flow rate of 5 μL min^{-1} was the smallest, due to heat diffusion (Figure S5b). Furthermore, the impact

64 of input power on thermal effect was considered. The pentagonal effective-piezoelectrical area of the

device was chosen as the region of interest (Figure S5c). As the input power increased, the average temperature of this area first increased and then stabilized. This stable average temperature was 150–170 °C. The maximum temperature at 2000 mW in this area was 166 °C, i.e., less than 218 °C, the boiling point of mineral oil (Figure S5d). The higher the power applied, the stronger the inverse piezoelectric effect induced, such that the heat generated from viscous attenuation of GHz BAWs and electromechanical losses of the device increased. This diffusion and expansion of heat affected the coalescence and growth of the bubble.

Figure S5 Acoustothermal effect of GHz BAWs in oil. (a) Distribution of oil temperature in the microchannel at an applied power of 2000 mW and flow rates of 0.1, 1 and 5 μL min^{-1}, respectively. The scale bar is 100 μm. (b) Areas of different isotherms at a power of 2000 mW and flow rates of 0.1, 1 and 5 μL min^{-1}, respectively. (c) Distribution of oil temperatures at different applied powers above the pentagonal BAW device. The scale bar is 50 μm. (d) Average oil temperature at different applied powers and flow rates above the pentagonal BAW device.

80
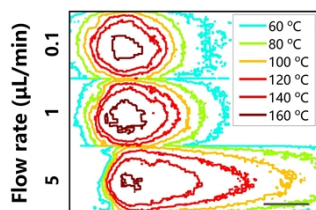
Figure S6 Isotherms at different temperatures and flow rates. The scale bar is 100 μm.

82

4 Performance of device driven by direct current

To delineate the role of acoustothermal effect during the phase of bubble nucleation, we effectively decoupled the thermal field from acoustic filed. A direct current (DC) was applied across the two ends of the bottom electrode (BE), whereas the top electrode remained unloaded, devoid of any electrical signal imposition (Figure S7b). Under these conditions, the heat generation was solely attributable to the Joule heating effect of BE, precluding the possibility of acoustic waves generation via the inverse piezoelectric effect. This experimental setup facilitated the decoupling of the thermal field from the acoustic field, while maintaining consistency in other experimental parameters. The temperature distribution was measured by the method in section 3 of Supporting Information.

When a voltage of 5 volts was applied to the device, the temperature reached within the pentagonal region through Joule heating was roughly equivalent to that achieved by the acoustothermal effect under a 2000 mW power input, as discussed in Section 3 in Supporting Information (Figure S7a). Scrutinizing the results revealed that, in this case, actuating the device for a duration of 15 s, exclusively under the influence of thermal effect, failed to induce bubble formation within the designated area (Figure S7c-f). In marked contrast, as illustrated in Section 3.2 in main text, bubble was formed within just 1 ms under the simultaneous presence of acoustic and thermal effects. Thus, these experimental findings substantiated that during the bubble nucleation stage, the dominant impetus was the acoustic wave, rather than the thermal effect. These results substantiated that bubble formation was a consequence of the effect induced by acoustic waves, rather than a result of heating or outgassing of the oil.
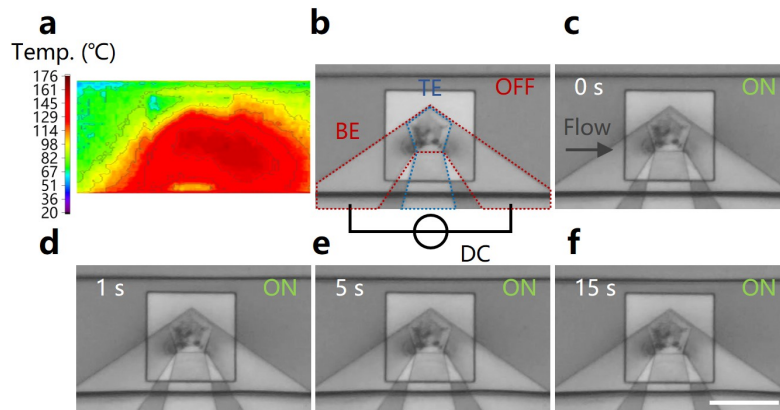
103
104 Figure S7. Performance of device driven by direct current in the oil. (a) The temperature distribution in the
105 microchannel induced by Joule heat. (b) The direct current (DC) was applied to both ends of the bottom electrode
106 (BE). While the top electrode (TE) did not work in this case. (c)-(f) The performance of device at 0, 1, 5, and 10 ms
107 when the power of DC was turned on. The scale bar is 100 μm.

108

109 5 Performance of device without nanostructural enhancement

110   To compare the extent to which a roughened surface facilitates onset, we conducted a control

111 experiment. Using a device without nanostructural enhancement, we applied 2500 mW of power and

112 monitored for bubble formation. As depicted in Figure S8, no bubble generation was observed within

113 30 s. Conversely, for nanostructurally enhanced device, bubbles were produced within 1 ms under the

114 power of 1585 mW. This finding underscores the pivotal role of a roughened interface in promoting

115 bubble generation under gigahertz acoustic waves.

116
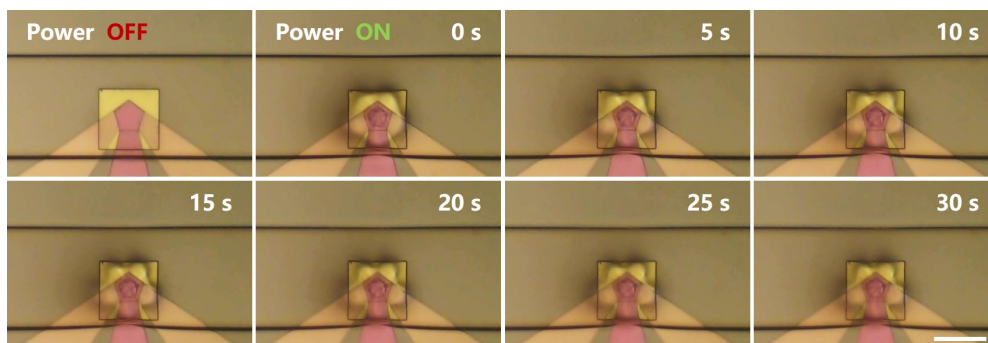
117
118   Figure S8. Performance of non-enhanced device. The scale bar is 100 μm.

119

120 6 Critical size of steady bubble

121   When the micro gas nuclei coalesced with each other to form a steady bubble, the single bubble

122 grew continuously supported by the acoustothermal effect. For the minimum surface free energy, the

123 steady bubble tended to be spherical by the interfacial tension. When the bubble touched the top of

124 microchannel, it would be confined by the ceiling, resulting in the decreased of growth rate. To

125 facilitate the calculation, the model of critical bubble was simplified. The size of critical steady bubble

126 depended on the size of device and the height of microchannel:

127 $R = (r^2 + h^2)/2h$

128 where R, r and h are the radius of steady bubble, the radius of incircle of pentagonal device, and the

129 height of microchannel respectively. In this hypersound acoustic system, the theoretical diameter of

130 critical steady bubble is 64 μm, which is constant with the experimental results.

131
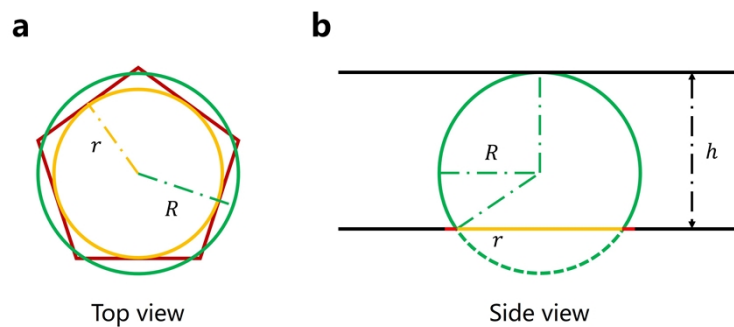
132

133 Figure S9. The schematic diagram of the critical steady bubble. (a) The top view above the device and   bubble. The
134 red pentagon represents the profile of acoustic device. The yellow circle is the incircle of pentagonal device. The
135 green circle represents the profile of steady bubble. r is the radius of incircle of pentagonal device. R is the radius of
136 steady bubble. (b) The side view of the device and bubble. The black lines represent the bottom and top of the
137 microchannel. h is the height of the microchannel.
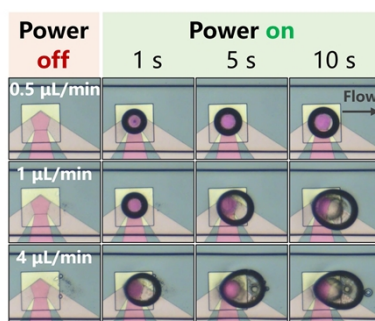
138

139 **7 Evolution of the bubble**

140
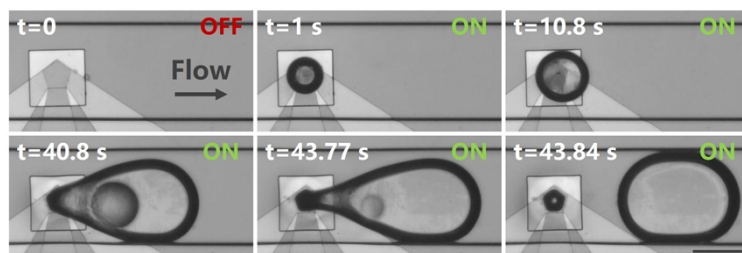
Figure S10. Evolution of the bubble when the device is continuously turned on. The scale bar is 100 μm.

8 Influence of flow rate on the bubble size

Figure S11. Steady bubble at different time points when the flow rate of oil was 0.1, 1 and 5 μL min^{-1} respectively. The scale bar is 100 μm.

9 Droplet splitting

Oil and water were infused into the microfluidic chip via syringe pumps. At the flow-focusing structure, the oil (continuous phase) separated the water (dispense phase) into discrete microdroplets. These water-in-oil microdroplets progressed downstream into the straight channel. Within the straight channel, stable bubbles were utilized to perform splitting operations on the microdroplets.
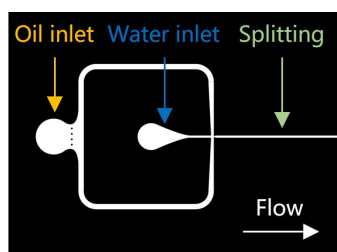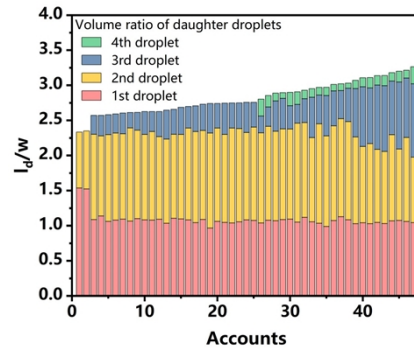

Figure S12. Structure of the microfluidic chip employed for the generation and splitting manipulation of droplets.

8

Figure S13. Volume ratio of daughter droplets versus different volume of mother droplets.